Flexible Array of High Performance and Stable Formamidium-Based Low-n 2D Halide Perovskite Photodetectors for Optical Imaging

Tao Wang[1] [#], Daming Zheng[1,2,3] [#] *, Karol Vegso[5,6], Nada Mrkyvkova[5,6], Peter Siffalovic[5,6], Xiaocong Yuan[1], Michael G. Somekh[1,4], Laurent Coolen[3]*, Thierry Pauporte[é]*, Feng Fu[1,7]*

1. Nanophotonics Research Center, Shenzhen Key Laboratory of Micro-Scale Optical Information Technology and Institute of Microscale Optoelectronics, Shenzhen University Shenzhen 518060, P. R. China.

2. Chimie ParisTech, PSL Research University, CNRS, Institut de Recherche de Chimie Paris (IRCP), UMR8247, 11 rue P. et M. Curie, F-75005 Paris, France.

3. Sorbonne Université, CNRS, Institut de NanoSciences de Paris, INSP, F-75005 Paris, France.

4. Faculty of Engineering University of Nottingham Nottingham NG72RD, UK.

5. Institute of Physics, Slovak Academy of Sciences, Dubravska cesta 9, 84511 Bratislava, Slovakia.

6. Center for Advanced Materials and Applications (CEMEA), Slovak Academy of Sciences, Dubravska cesta 5807/9, 84511 Bratislava, Slovakia.

7. Research Center for Humanoid Sensing, Zhejiang Lab, Hangzhou 311100, China.

*Correspondence: daming.zheng@chimieparistech.psl.eu; laurent.coolen@insp.jussieu.fr; thierry.pauporte@chimieparistech.psl.eu; fufeng@szu.edu.cn.

Author Contributions

[#]The authors contributed equally to this work

Abstract: Metal halide perovskites are attracting increasing attention as photodetectors (PDs) materials due to their excellent photoelectric properties. However, integrating perovskite to realize high-resolution perovskite pixel arrays remains critical to enable practical devices. Herein, we demonstrate a high-responsivity and stable 10×10 flexible PDs array based on formamidium-based quasi-2D Ruddlesden-Popper $(BA)_2FAPb_2I_7$ (n=2) (BA= butylammonium, $C_4H_9NH_3^+$) perovskite elements for image sensing. The high-performance $(BA)_2FAPb_2I_7$ arrays are synthesized on a polyethylene terephthalate (PET) flexible substrate, on a large scale, high quality, and controllable manner by introducing Au nanoparticles to enhance film quality upon the annealing process and recrystallization by applying formamidium chloride (FACl) post-treatment to reduce perovskite film defects, combined with an innovative SiO_2-assisted

hydrophilic and hydrophobic surface treatment strategy. The prepared flexible PDs arrays show excellent optoelectronic properties with high responsivity (5.9 A W^{-1}), a detectivity of 8.2×10^{12} Jones, large on/off current ratio (up to 3×10^4), ultimate response speed (12.8 μs/10.1μs), and wide spectral response range. In addition, the device shows outstanding mechanical stability under severe bending (θ=120°) and excellent folding durability after thousands of bending cycles. It also exhibits excellent environmental stability with only a slight degradation of photoresponse after 100 days of storage under the ambient environment. Finally, the integrated flexible PDs arrays can be used as an effective visible light image sensor with good spatial resolution, paving a multifunctional and competitive way for future wearable sensors and artificial vision systems.

One-sentence summary: Low-dimensional halide perovskite layers pixelized on a polyethylene terephthalate (PET) flexible substrate provide high performance photodetectors.

Keywords: Quasi-2D halide perovskite; Au nanoparticles; Flexible photodetectors arrays; High-responsivity; Imaging.

1. INTRODUCTION

Photoelectronic devices such as photodetectors (PDs), solar cells (SCs), light-emitting diodes (LEDs), and lasers have found a wide range of applications in industry, science, and daily life[1-8], e.g. optical communication, imaging technology, chemical/biological monitoring, digital displays and biorobots[9-13]. With the development of the new optoelectronic industry, flexible optoelectronic devices have attracted more and more attention due to their advantages of lightweight, portability, wearability, and low manufacturing cost [14, 15]. In particular, the interest for electronic eyes and wearable scanners continues to increase, spurring the ongoing pursuit of expandable, high-resolution, and full-color wide-angle flexible PDs [13, 16, 17]. Among various PDs materials, lead halide perovskite, as a promising semiconductor material, is an excellent choice for optoelectronic device applications with high-resolution, good stability and broad spectral response due to its ultra-wideband detection, tunable band gap, fast response, low cost and easy processibility [18-21]. Owing to the incompatibility of perovskite materials with traditional photolithography technology and polar solution stripping [22, 23], how to miniaturize and integrate them while ensuring the high photoelectric performance of flexible perovskite devices remains an important technical challenge that has a crucial impact on device miniaturization and image quality.

In order to realize array integration of perovskite-based PDs with excellent flexibility, high-resolution, and satisfactory mechanical adaptability, many researchers have focused much effort on controllable synthesis of materials and the design of devices. Currently, some

advanced photolithography technologies for direct top-down patterning device fabrication, such as laser-induced growth, focused ion beam etching, and inkjet printing [24-26], often require very complicated instrumentation and equipment and are difficult to handle on flexible substrates. In addition, laser and focused ion beam irradiation can cause unavoidable damages, making them unsuitable for large-scale fabrication of flexible perovskite PDs arrays. In contrast, prefabrication of templates/patterns on a flexible substrate by a modified bottom-up photolithography method is easy to process and versatile [2, 27]. In this method, an auxiliary layer is usually combined with photolithography. Compared with other photolithographic preparation methods, the major advantages of the modified photolithographic one are high-resolution, easy fabrication of templates, and good alignment with patterned electrodes [1, 12, 15]. In addition, the crystal quality can be easily improved by precisely adjusting the perovskite growth process in the template. Therefore, this method has great potential for large-scale integration of perovskite devices. For example, Zhu *et.al*[28] and Pan *et.al*[1] have successfully demonstrated that $CH_3NH_3PbI_{3-x}Cl_x$ perovskite can be patterned by photolithography, which offers the possibility of large-scale integrated PD arrays. Although some flexible PDs arrays based on organic-inorganic perovskite films have already been described using the photolithography method, the performance of organic-inorganic 3D hybrid perovskite degrades rapidly due to their susceptibility to moisture in the environment, which seriously hinders their practical application [29, 30]. On the other hand, quasi-2D perovskites display excellent environmental stability. In particular quasi-2D perovskites based on formamidinium (FA^+) exhibit better structure and thermal stability than those based on methylammonium (MA^+) [20, 31, 32], and have a better band gap and charge transfer capability, making them an ideal photosensitive material for the preparation of highly potent and stable PDs[33, 34]. To date, there are only a few reports on the patterned growth of quasi-2D FA-based perovskite within PDs[17, 35]. This is because the nucleation and crystallization processes cannot be controlled, which leads to poor film morphology and crystallinity of perovskite, thus affecting the photoelectric performance [36-38]. Therefore, it is urgent to further explore the controllable growth of quasi-2D perovskite materials and fabricate stable and high-resolution flexible perovskite-based PD arrays for image sensing.

Here, we present a 10 × 10 flexible perovskite PDs array using stable quasi-2D Ruddlesden-Popper $(BA)_2FAPb_2I_7$ (n=2) films as photosensitive material on a polyethylene terephthalate (PET) substrate. It has been used as a demonstrator of an image sensor. To satisfy the PDs arrays' need for independent photosensitive units, we propose two treatments which have greatly improved the photoelectric response of the films: (i) we introduced Au nanoparticles (referred to as Au_NPs) to reduce film defects and grain boundaries and improve crystallinity, and (ii) we used formamide chloride (referred to as FACl) as an efficient recrystallization agent to reduce recombination center and promote the correct crystal

orientation of the film. Combined with the developed SiO_2-assisted hydrophobic and hydrophilic treatment process, a controllable synthesis of large area $(BA)_2FAPb_2I_7$ (n=2) perovskite film arrays with precise pixel position and controllable morphology was achieved. The flexible PDs array exhibited excellent optoelectronic properties with high responsivity, large on/off current ratio, and broad spectral response. This set of detection properties is among the best reported for quasi-2D perovskite devices. In addition, the device shows excellent electrical stability under severe bending (θ=120°) and excellent folding durability after thousands of bending cycles. It also exhibits excellent environmental stability with only a weak degradation in photoresponsivity after 100 days of storage under ambient conditions. Moreover, the flexible quasi-2D perovskite PDs array can work as a broadband light sensor for ultraviolet (UV), visible (vis) and near-infrared (NIR) light with homogenous photoreaction of all pixels.

2. RESULTS

Flexible quasi-2D $(BA)_2FAPb_2I_7$ perovskite PDs arrays were fabricated by a modified photopatterned polymer template photolithography method. The overall structure of the large-area flexible PDs arrays is shown in **Fig. 1a**. The device consists of 10 × 10 individually addressable pixels and contains five layers of material supported on a PET substrate: Au electrodes, an auxiliary SiO_2 layer, a perovskite film, and a PMMA film for encapsulation. The most critical part of the fabrication process was that each perovskite film had to be grown in the hydrophilic region to form an array in which the interdigitated electrodes were exposed to etching of the covered SiO_2 film. The fabrication process for the flexible PDs arrays is detailed in **Fig. S1** of the Supporting Information. SEM images of the designed electrode and the optical image of 10 × 10 pixelated flexible PDs arrays are shown in **Fig. 1b** and **Fig. 1c,** respectively. All pixels share a common electrode platform, and each pixel has a separate electrode with a size of 200 × 200 μm. **Fig. 1d** shows the SEM image of the perovskite array, which has a regular and uniform shape with sharp edges and a compact surface. However, in order to achieve a more stable quasi-2D perovskite, it was obtained based on the dimension reduction of 3D perovskite. During this process, the periodic metal was damaged, because part of the electron donor defects or hole acceptor defects have low energy levels in perovskite. Dielectric and quantum confinement are well-known phenomena in quasi-2D perovskite multi-quantum well structures, which greatly expand the exciton binding energy and limit the charge transport within the quantum well plane[39, 40]. This usually leads to the reduction of diffusion length and carrier mobility of quasi-2D perovskite materials [18, 41, 42]. As a result, the quasi-2D perovskite exhibited poor photoelectric performance due to its poor carrier transport compared to 3D perovskite. To overcome this challenge, while achieving long-term stability and high-performance, the most effective methods are additives as dopants and/or recrystallization of the films to passivate defects [31, 43, 44]. Therefore, inspired by our previous works [31, 45, 46],

we used Au_NPs as dopants to reduce defects and grain boundaries, and then we used FACl as a recrystallization agent to improve crystallinity and passivate defects of the perovskite films. **Fig. 1e** shows the main synthesis process of the $(BA)_2FAPb_2I_7$ perovskite film. The surface of the modified film was smooth and without any pinholes, as seen on the enlarged SEM images (**Fig. 1d**). Considering that increasing the thickness of perovskite film increases the risk of material failure under deformation, we chose a thickness of 200 nm for the PDs. In addition, in order to test the versatility of the patterning process, perovskite arrays with various geometric shapes, including circular, triangular, and alphabetical patterns, were fabricated with the same preparation method (**Fig. 1f**).
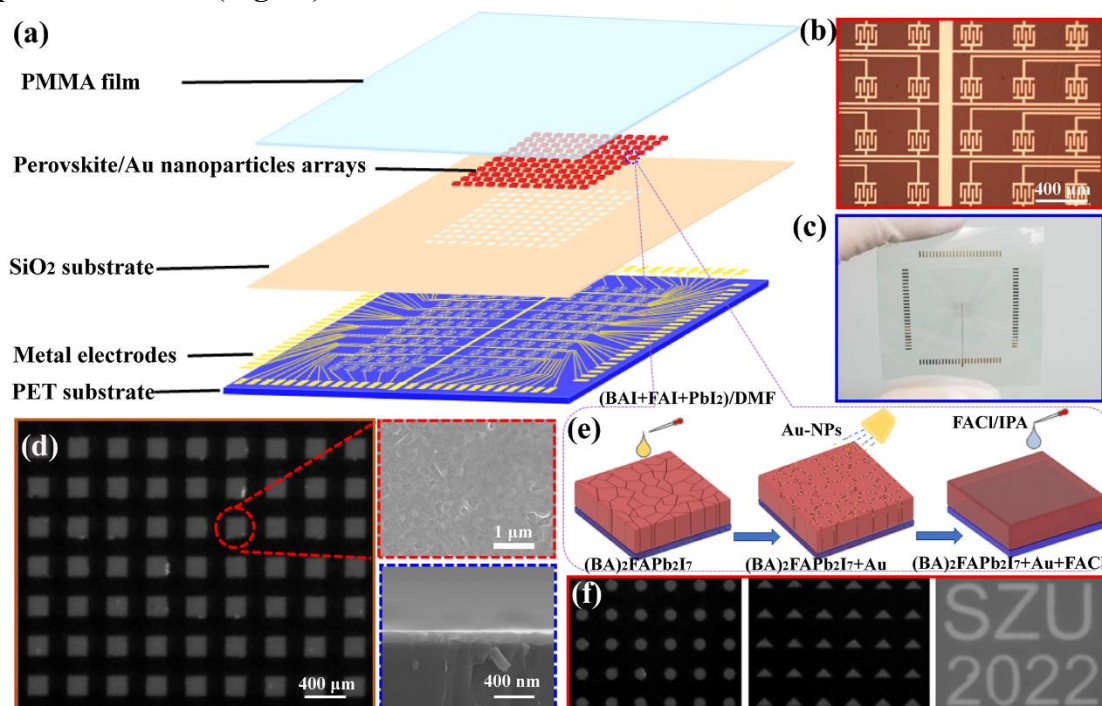

Fig.1. Schematic illustration of the device structure and fabrication process. (a) Schematic structure of the device. **(b)** Optical image of Au electrode. **(c)** Photograph of 10×10 pixelated flexible PD arrays. **(d)** SEM images of patterned perovskite arrays and magnified SEM images of the film surface and cross-section. **(e)** Schematic illustration of synthesis process by introducing Au-NPs and FACl-recrystallized perovskite film. **(f)** As-grown perovskite arrays with different geometries, including circular, triangular, and alphabetical patterns.

The PDs are based on the $(BA)_2FAPb_2I_7$-Au_NPs-FACl perovskite (denoted as PD3), as shown in **Fig. 2a**. To optimize the photoelectric performance of the PVK-Au_NPs-FACl-PDs, we first investigated the sputtering time of Au_NPs and the concentration of FACl. We found an optimal sputtering time of Au_NPs at 15 s and a FACl concentration at 2 mg mL^{-1} dissolved in isopropanol (IPA) solution. More details on the optimized fabrication process of PD3 can be found in the Supporting Information.
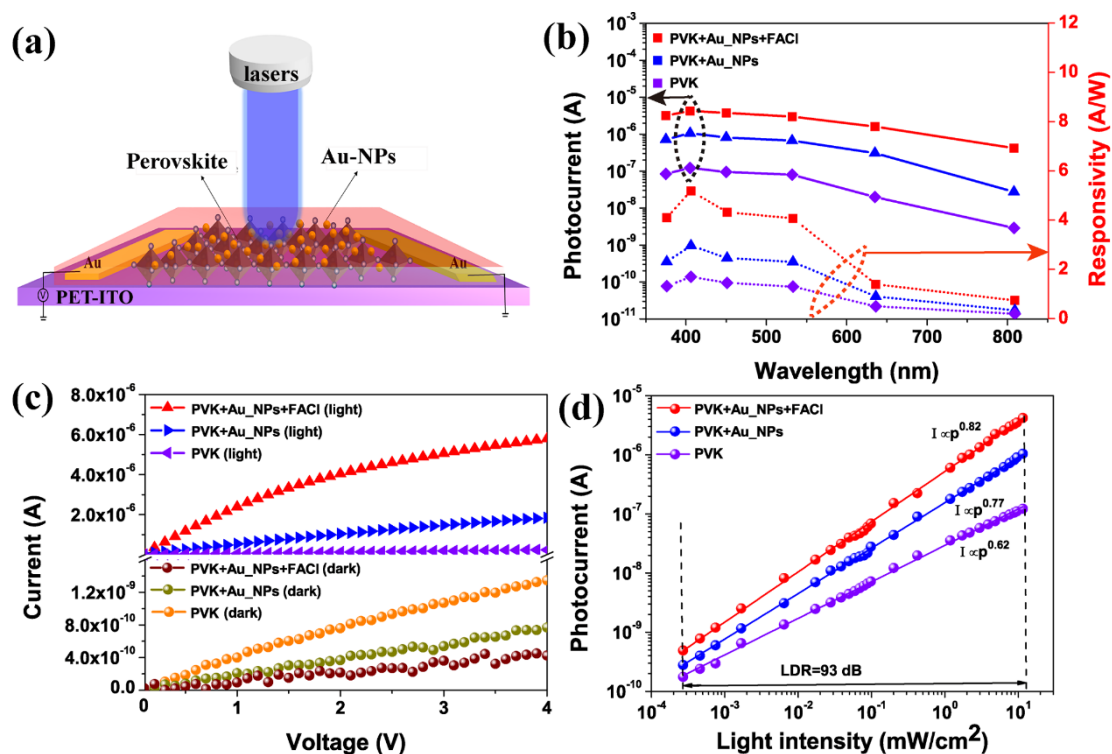
Fig.2. Device structure and photodetection performance. (a) Schematic diagram of the device**. (b)** Photocurrent (illumination power density of 11.52 mW cm^{-2}) and responsivity (illumination power density of 0.27 μW cm^{-2}) of the 3 devices as a function of the illumination wavelength at 2 V bias. **(c)** *I-V* curves of the 3 devices under dark and 405 nm illumination. **(d)** Photocurrent as a function of light intensity at 2 V bias.

(**Fig. S3** and **S4**). The photoresponse of a single pixel was investigated to evaluate the optoelectronic performance of the PDs array and compare the three types of devices. **Fig. 2b** shows the photocurrent (with a light intensity of 11.52 mW cm^{-2} and a bias voltage of 2V) and photoresponsivity (R) (at a light intensity of 0.27 μW cm^{-2} in order to avoid saturation effects, and under a bias voltage of 2V) of the three devices under different wavelength of monochromatic illuminations. The responsivity R is given by the equation [31, 47]:

$$R = \frac{I_{light} - I_{dark}}{PS} \tag{1}$$

where I$_{light}$ is the photocurrent, I$_{dark}$ is the dark current, *P* is the power density of light, and *S* is the effective light-irradiation area. As shown in **Fig. 2b**, the device had a higher photocurrent in the blue UV-vis region compared to the red region, with a maximun around 405 nm. Moreover, the photocurrent of PD3 was higher than that of PDs based on the (BA)$_2$FAPb$_2$I$_7$ perovskite (denoted as PD1) and PDs based on the(BA)$_2$FAPb$_2$I$_7$-Au_NPs perovskite (denoted as PD2) over the whole spectral region, by a factor 35 and 4, respectively, showing the superiority of the PD3 device in terms of detection efficiency. Consequently, the responsivity of the PD3 device (**Fig. 2b**) was optimal in the blue domain, and significantly higher than for the PD1 and PD2 devices. For instance, PD3 showed about three times higher responsivity than

6

for PD1 at 405 nm (**Fig. S5d**). The higher photocurrent and responsivity of PD3 may be attributed to the introduction of Au_NPs into the perovskite to improve the quality of film formation and reduce the density of defect states (**Fig. S6**, details in the Supporting Information), and to the recrystallization of the perovskite by using FACl as a recrystallization agent to improve the crystallinity. In this way, the device could have excellent light absorption and high carrier mobility (**Fig. S6**, details in the Supporting Information), leading to better photoelectric performance. To evelute the photoresponse of modified PDs compared to the pristine PDs, the *I-V* curves with and without illumination (405 nm, 11.52 mW cm^{-2}) were measured, as shown in **Fig. 2c**. At a bias voltage of 2 V, compared with the PD1, the PD3 show more than 300 times higher photocurrent (4.0 µA), which is almost comparable to the reported 3D MAPbI$_3$ perovskite photodiodes. For example, Chen *et al*. prepared flexible PDs based on the MAPbI$_3$ and obtained photocurrent of 8 µA under 365 nm light and a bias voltage of 2 V[48]. For lower voltages, the current changes linearly with voltage, indicating an ohmic contact between the perovskite and metal electrodes. As for the dark current or leakage current, it was reduced by a factor 3 for PD3 compared to the pristine PDs, perhaps because the perovskite was recrystallized by the introduction of Au_NPs and FACl and had fewer grain boundaries and high-quality crystallinity, resulting in a film with fewer defect states[49]. The dark value of the device at a bias voltage of 2 V was only 2.0×10^{-10} A, while photocurrent increased to 4.0×10^{-6} A at an illumination intensity of 11.52 mW cm^{-2} (**Fig. S7a**).

The linear response of the device to light intensity is key for optical imaging and communication applications[50, 51]. **Fig. 2d** shows the relationship between the photocurrent and the light intensity of those devices. The log-log curve is linear, indicating a power-law dependence. For PD1, the exponent was only 0.62, while it increased up to 0.82 for PD3, much closer to the unity exponent expected for a fully linear response. The response range of the device to incident light intensity was measured from 0.27 µW cm^{-2} to 11.52 mW cm^{-2}, and the corresponding quasi-linear dynamic range was about 93 dB, which is similar to the perovskite PDs reported previously[50, 52].
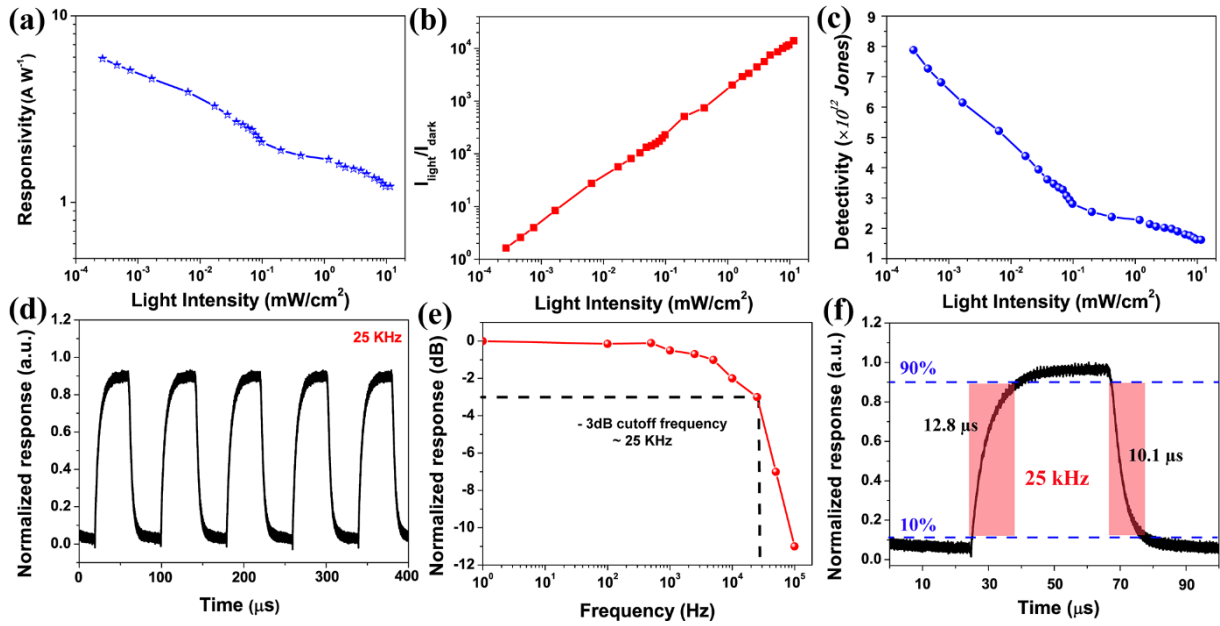
Fig. 3. Characterization of photoelectric properties of PVK-Au_NPs-FACl-PDs (PD3). (a) Responsivity, **(b)** I_{light}/I_{dark} and **(c)** detectivity as a function of the light intensity under 405 nm illumination under a bias of 2 V. **(d)** Temporal photoresponse under square wave optical signal illumination at a frequency of 25 kHz. **(e)** Normalized photoresponse versus the input signal frequency to estimate the 3 dB cutoff frequency of device. **(f)** An individual photoresponse curve at 25 kHz.

As shown in **Fig. 3a**, the R value of PD3 decreases slightly (by a factor 5 over > 4 decades) with the increase of power density, while it would remain constant if the PDs response was fully linear. This phenomenon is consistent with data reported in the literature on PDs. [48, 53] This is due to the fact that the Auger process shortens the lifetime of photoinduced charge carriers or to the saturation of trap states at high photon flux [54]. The relationship can be expressed according to equation (2) [55]:

$$\Delta I = (\eta P_{in} \frac{q}{\hbar\omega})(\frac{\tau_{lifetime}}{\tau_{transit}})$$ (2)

where $\Delta I = I_{light}$-I_{dark} is the current gain, η is the photoelectric conversion efficiency, and $\tau_{lifetime}/\tau_{transit}$ is the photoconductive gain. In general, $\tau_{transit}$ is constant, as determined by the carrier mobility, voltage, and channel length in perovskite. In this case, the photoinduced carrier lifetime $\tau_{lifetime}$ decreases with the power density of the incident light. A longer lifetime obtained at lower power density leads to a higher photoconductivity gain. When the trap states are fully occupied, more photocarriers are excited at higher light power density. As the scattering rate increases, the average lifetime of the carrier decreases. Therefore, increasing the incident light power density leads to higher photoinduced carrier concentration and recombination rate. As a result, the R value of the device decreases as a function of the illumination intensity.

The I_{light}/I_{dark} current ratio of the PD3 under different voltage was further characterized. The pronounced response of the device to light is remarkable. The highest I_{light}/I_{dark} ratio of up

to about 2×10^4 was achieved at an illumination power density of 11.52 mW cm^{-2} and at a bias voltage of 2 V (**Fig. 3c**), which is comparable to other perovskite PDs (**Table 1**). In contrast, the highest I_{light}/I_{dark} of PD1 and PD2 were about 2.0×10^2 and 2×10^3, respectively (**Fig. S7b**). We have fabricated at least three devices of each type to ensure good reproducibility. The results are shown in **Table S1**, and the I_{light} and I_{dark} values of each type of the devices are almost the same with only 5-10 % differences.

Detectivity (D*) is a measure of the detector sensitivity, limited by the shot noise of the dark current, which is the major component of the total noise. $D*$ can be calculated according to equation (3)[56]

$$D^* = \frac{R}{\sqrt{\frac{2qI_{dark}}{A}}} \qquad (3)$$

where q is the electronic charge, and A is the area of the PDs. With the addition of Au_NPs and after recrystallization using FACl, the film becomes denser and has a better crystallinity, and the dark current of the modified PVK-Au_NPs-FACl-PDs was reduced to the lowest value of 10^{-10} A. The combination of the suppressed dark current and the improved photocurrent contributes to an ultrahigh detectivity of 8.2×10^{12} Jones under 2V bias (405 nm, 0.27 mW cm^{-2}). This value is among the highest reported for quasi-2D perovskite PDs, as listed in **Table 1**. It decreased only by a factor 4 as the light power density was increased by more than 4 decades up to 11 mW cm^{-2} (**Fig. 3c**).

In addition, the response rate of the device to light pulses of different frequencies was investigated. **Fig. 3d** shows the temporal photoresponse of the device at a frequency of 25 kHz. The device had a stable temporal response to pulsed signals with frequencies ranging from 1 to 100 kHz. According to the normalized response frequency curve (**Fig. 3e**), the 3dB cutoff frequency (f_{-3dB}) of the device was at 25 kHz, which was almost in the same order of magnitude as the reported for MAPbI$_3$-PDs. For example, Huang *et al.* prepared dual-band PDs based on the MAPbI$_3$/MAPbBr$_3$ with a response bandwidth (f_{-3dB}) of ~33 kHz[30]. Huang *et al.* by a Cu-doping strategy, prepared PDs based on MAPbI$_3$ with a response bandwidth of 50 kHz[50]. In the single response cycle curve of 25 kHz (**Fig. 3f**), the response time and decay time of the device were 13 and 10 µs, respectively, which are much faster than the response and recovery speed of the human eyes[57, 58]. Overall, the responsiveness and response speed of the device were better compared with the previously reported PDs, as shown in **Table 1**. Therefore, our methods is competitive in enhancing the device performance.
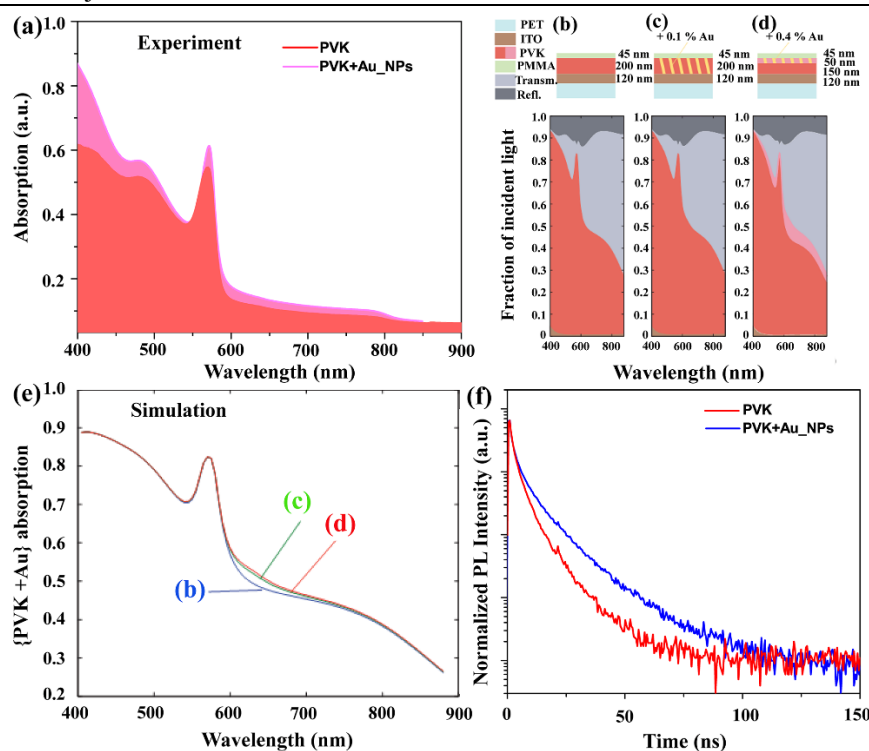
Fig. 4. Optical properties measurement and theoretical simulation of PVK and PVK+Au_NPs. (a) Absorption spectra of PVK and PVK+Au_NPs. **(b-d)** Transfer-matrix-simulated optical reflection, transmission, and absorption for PVK, PVK+Au_NPs (Au_NPs volume fraction 0.1%), and PVK+ Au_NPs (Au_NPs volume fraction 0.4%). **(e)** Combined optical absorption spectra from (b-d). **(f)** Time-resolved PL curves of PVK and PVK+Au_NPs (excited at 405 nm).

The combination of Au_NPs addition and FACl treatment with perovskite films clearly resulted in a significant photoelectric properties improvement. To understand the effect of Au_NPs and FACl treatment on the formation process and to elucidate the crystal growth mechanism of the perovskite film, we used transfer-matrix simulation calculation, glow discharge-optical emission spectroscopy (GD-OES) and grazing-incidence wide-angle X-ray scattering (GIWAXS) techniques.

First, regarding the effect of Au_NPs, many reports attribute the enhanced photocurrent to improved light absorption in the perovskite layer due to localized surface plasmon resonance (LSPR) and light scattering [45, 59-61]. **Fig. 4a** shows the measured absorption spectra of the pure perovskite film and film with added Au_NPs. Measured spectra were similar to those of typical perovskite films, with an absorption edge at about 580 nm. The introduction of Au_NPs improves slightly the film absorption (except in the 400-500 nm range, where uncertainties may be high due to low transmission). A comparison of the pure perovskite and added Au_NPs samples shows that the enhancement occurs throughout the absorption spectrum. No pronounced plasmonic absorption peak corresponding to the LSPR effect was observed. To clarify this, we calculated the optical properties of perovskite film with added Au_NPs with a

10

diameter of 14 nm (inset of **Fig. S3a**). We used the transfer-matrix formalism to describe the multi-layer device [62] and described the perovskite containing Au-NPs as an effective medium. We first modelled light absorption by the pure perovskite (**Fig. 4b**). We then considered the addition of Au_NPs, with two hypotheses on the spatial distribution of Au_NPs, either homogeneously distributed within the perovskite layer thickness or remaining on the top. In the first one (**Fig. 4c**), the Au_NPs were uniformly distributed throughout the perovskite layer, and in the second one (**Fig. 4d**), the Au_NPs were distributed in the upper 50 nm layer of the perovskite. Details of the estimated Au_NPs volume fraction are provided in the Supporting Information. The resulting absorption by the PVK+ Au_NPs layer (**Fig. 4e**) was only very weakly affected by the presence of Au_NPs, because the Au_NPs concentration was too low to modify the perovskite optical properties. Moreover, it can be seen in **Fig. 4e** that the distribution of Au_NPs at different positions had no effect on the light absorption of the samples, the absorption edge did not shift. We also observed that the light absorption was slightly enhanced due to the reflection of light by the Au_NPs present at the surface, after it crosses the perovskite layer.

We also measured the thermal conductivity of the pure perovskite film and film with added Au_NPs to further demonstrate that the addition of Au_NPs contributes to better crystallization of the perovskite film. As shown in **Fig. S8**, the thermal conductivity of perovskite film added with Au_NPs is about 52 % higher than that of pure perovskite, indicating that the presence of Au_NPs makes perovskite film more uniformly heated upon the annealing process, thus contributing to a better crystallization [63-65] (see details in the Supporting Information). Moreover, the PL decay profiles of the $(BA)_2FAPb_2I_7$ perovskite film without and with the presence of Au_NPs are shown in **Fig. 4f**. The PL decay data were fully fitted with a biexponential function, and the results are shown in **Table S3**. τ_{slow} is related to bulk recombination and then to defect density. We observed two important phenomena: the τ_{slow} of the pure perovskite was 33.8 ns, whereas the τ_{slow} of Au_NPs was much longer 63.2 ns. This increase suggests that the structural quality of perovskite was greatly improved in the presence of Au_NPs in agreement with our previous work [45]. The addition of a suitable amount of Au_NPs increases the grain size and reduces grain boundaries rich in defects that act as recombination centers. It also improves the bulk quality of the perovskite and reduces inherent defects[66-68]. The improved structure of perovskite film also has a positive effect on the photoinduced charge carrier migration and separation, so the modified device should have a better photoelectric performance.
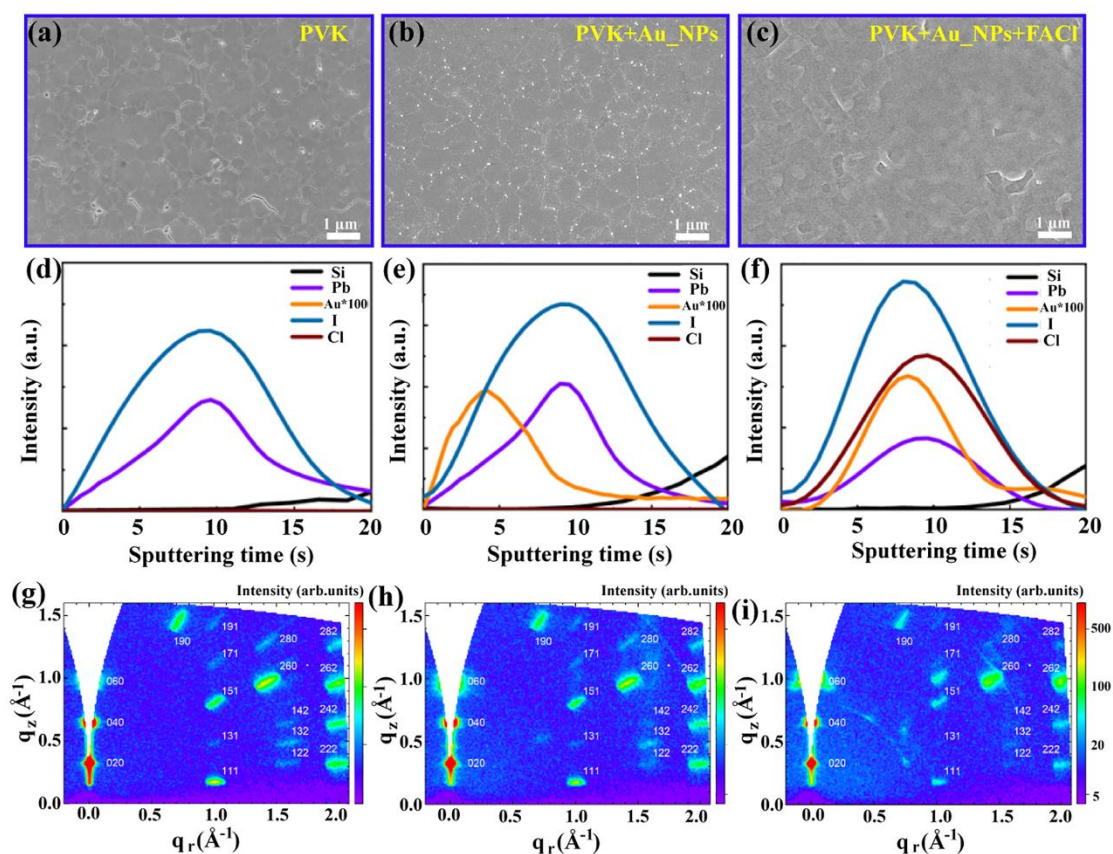
Fig. 5. SEM images, profile of the main elements in the perovskite film, and GIWAXS patterns characterizations. Top-view SEM images of the **(a)** pure PVK, **(b)** PVK+Au_NPs, and **(c)** PVK+ Au_NPs +FACl films. GD-OES distribution curves of the main elements composing the **(d)** pure PVK, **(e)** PVK+Au_NPs, and **(f)** PVK+ Au_NPs +FACl films. GIWAXS patterns of **(g)** pure PVK, **(h)** PVK+Au_NPs, and **(i)** PVK+ Au_NPs +FACl films.

SEM images of the samples are shown in **Fig. 5a-c**. For the pure perovskite (**Fig. 5a**), the presence of grooves and large pinholes on the film surface was visible. After the addition of Au_NPs (**Fig. 5b**), the quality of the film was significantly improved as it showed no defects such as pinholes and grooves. Moreover, the Au_NPs were mainly distributed in the grain boundary. We assume that Au_NPs act as the recombination centers for photogenerated electrons and holes at the grain boundaries, consistent with a shorter PL lifetime compared to the pristine films. When FACl was used as a recrystallization agent, the crystal quality of the film was significantly increased, and the micrometer-sized grains were assembled smoothly without pinholes. The surface after FACl recrystallization shows better coverage compared to the pristine one. Atomic force microscopy (AFM) was used to measure the roughness of the perovskite films (**Fig. S9**). The root-mean-square (RMS) roughness of the film decreases from an initial 41 nm to 28 nm after modification. These values were consistent with SEM imaging. We analyzed the absorption edge using the Tauc plots in **Fig. S10d**. Considering a direct bandgap, the intersection of the linear fit with the energy axis yielded optical band gaps of

2.11eV, 2.10 eV, and 2.09 eV for PVK, PVK+Au_NPs, and PVK+Au_NPs+FACl, respectively. The essentially unchanged bandgap value indicates that the introduction of Au_NPs and recrystallized FACl did not cause a significant change in the perovskite lattice.

The *ex-situ* GD-OES technique was used to track the distribution of Au and other major elements in the perovskite layer to understand the influence of Au_NPs and FACl on the film formation process [65]. The GD-OES schematic is shown in **Fig. S11.** Through the distribution of these elements, we were able in our previous work to better understand the crystallization process and the quality of crystals [45, 69]. In **Fig. 5d-f**, the curve intensity shows the variation of the major element concentration in the perovskite with Ar plasma sputtering time. The sputtering time to completely probe the depth of perovskite layer (from top to bottom) was 20 seconds. As shown in **Fig. 5e**, when Au_NPs were introduced into the perovskite, the concentration of Au element curve first increased with the increase of sputtering time and then slowly decreased, indicating that Au was mainly distributed near the surface and in the upper part of the whole perovskite layer. Furthermore, it suggests that some Au_NPs can penetrate into the perovskite layer upon the annealing process. After FACl recrystallization (**Fig. 5f**), the I and Cl elements were discovered prior the Au element, suggesting that the recrystallization effect incorporates the Au_NPs into the perovskite layer. Combined with SEM results (**Fig. 5b and 5c**), we can conclude that the Au_NPs had a positive effect on crystallization of the perovskite throughout the preparation process. For Cl ions fate, we found that, after FACl post-processing, their concentration increased, first, and then lowered with the increase of sputtering time, indicating that Cl element was distributed throughout the perovskite layer and plays a key role in the recrystallization of the perovskite [43]. In addition, the crystal structure and grain orientation of the perovskite films were also investigated using GIWAXS. GIWAXS patterns of the pristine and modified perovskite films are displayed in **Fig. 5g-i**. Quasi-2D perovskite $(BA)_2FAPb_2I_7$ crystallizes in the orthorhombic space group (*Cmcm*,65). GIWAXS patterns were indexed using lattice parameters determined by single-crystal X-ray diffraction [67]. A distinct series of 020, 040, and 060 diffraction Bragg spots along the q_z direction confirms a uniaxial texture with the (010) lattice plane being parallel to the substrate. The orientation of the unit cell and the highlighted (020) and (111) planes can be seen in **Fig. S12**, illustrating the quantum well orientation with respect to the substrate. This crystallographic orientation was crucial for an efficient transport of electron-hole pairs along the quantum wells since the photodetection used here was based on in-plane geometry, which was in stark contrast to the typical orientation preferred in solar cells with perpendicular charge transport. Furthermore, non-coplanar diffraction spots in the higher reciprocal space exhibit narrow radial intensity profiles, indicating a highly textured growth of the crystalline perovskite layer. The elongation of the diffraction spots was due to the large sample interaction path projected onto the X-ray detector. As expected, the deposition of Au_NPs did not change the intensity or the radial position of the

diffraction spots. The inclusion of Au_NPs into perovskite layer during recrystallization with FACl also had no adverse effect on the crystalline texture, as the GIWAXS pattern remained essentially unchanged. This indicates an important fact, namely that Au_NPs presumably segregated at the grain boundaries. Therefore, we can conclude that Au_NPs and FACl-treatment significantly affect the properties of perovskite film. The enhanced structure of perovskite film can act as a continuous charge transport channel to achieve efficient charge transport and further extraction, contributing to the improvement of the device photoelectric performance.

To illustrate that the PDs with PVK+Au_NPs+FACl structure can generate higher photocurrent, the structure and energy band diagram are shown in **Fig. S13a** and **S13b**, respectively. Due to the inter-band absorption, photocurrent mainly arises from the dissociation of bound electron-hole pairs between the valence and conduction bands [56, 70]. The arrangement of the energy bands was analyzed by ultraviolet electron spectroscopy (UPS). The lowest unoccupied and the highest occupied molecular orbital (HOMO) levels of PVK, PVK+Au_NPs, and PVK+Au_NPs+FACl are shown in **Fig. S14**. The HOMOs difference between them was small, and the photocarriers generated by the PVK+Au_NPs+FACl layer can be well transmitted between layers. With the energy level matching and tight combination of thin films, photogenerated carriers can be extracted rapidly, thus achieving high responsivity of devices.

Table 1 Comparison of the characteristic parameters of published quasi-2D perovskite-based PDs.

Device structure	R [A W^{-1}]	D* [Jones]	Rising/falling time	On/off	Wavelength (nm)	Stability	Ref.
(HFA)$_2$FAPb$_2$I$_7$	0.95(10V@475nm, 8 mW/cm^2)	3×10^{11}	310/520μs	10^3	365-650	> 60 days	[71]
BA$_2$PbI$_4$–BA$_2$MAPb$_2$I$_7$	8.12(30V@460nm,50 μW/cm^2	1.5×10^{12}	----	> 10^2	400-700	----	[72]
In/GaN-Cs$_2$AgBiBr$_6$/Ag	1.46(0V@265nm,0.005mW/cm^2	9.4×10^{12}	3.46/8.44 ms	10^4	265	3 months	[52]
(iBA)$_2$(MA)$_3$Pb$_4$I$_{13}$	0.4 (1.5 V@532 nm, 1 mW·cm^{-2})	1.68×10^{12}	43 ms/22 ms	10^2	532	> 9 days	[73]
Au/2D FAPbI$_3$/Au	3.27(9V@645nm,18 nW)	1.35×10^{12}	0.35/0.54 ms	----	<815	>1400 s	[74]
ITO/PTAA/PEAI/3D perovskite/2D perovskite/C60/BCP	0.53(-0.1 V@900 nm, ---)	2.07×10^{11}	35 ns	---	300-1050	> 280 h	[75]
Graphene/MoS$_2$/(PEA)$_2$SnI$_4$/graphene	0.121 (0 V, @700 nm 5.46 nW/cm^2)	8.09×10^9	34 ms/38 ms	500	400-800	> 1000 s---	[76]
(BA)$_2$FAPb$_2$I$_7$ single-crystal	5(@-10 V,488nm, 3.5 μW/cm^2)	3.5×10^{11}	< 20 ms	---	488	>70 min	[77]

ITO/PEDOT:PSS/ (PEA)$_2$(MA)$_2$Pb$_3$I$_{10}$: AuAgNPrisms@SiO$_2$/ PCBM/PFN/Ag	7.15(0.3V@532nm, 10^{-4} mW/cm^2)	3.2× 10^{13}	4.0/5.8 ms	----	300-800	----	[78]
Au-nanograting/ PEDOT:PSS/(BA)$_2$FAPb$_2$I$_7$:FACl/C8BTBT	2.3(2V@405 nm,0.25µW/cm^2)	3.2× 10^{12}	9.74/8.91 µs	---	370-1100	>1000 h --	[31]
(BA)$_2$FAPb$_2$I$_7$+ Au_NPs+FACl	5.48 (2V @405 nm, 0.27 µW/cm^2)	8.2× 10^{12}	12.8/10.1 µs	2× 10^4	405-808	>100 days	This work

The stability of flexible perovskite-based optoelectronic devices has always been a challenge. We have investigated the photoelectric performance of flexible devices under bending stress. A cyclic bending test of the device was performed at a bending angle of 120°. As shown in **Fig. 6a,** after 10000 bending cycles, the photocurrent of the device was reduced by only 16%, and the device had stable optical switching characteristics. The on/off switching was still reproducible over several cycles (**Fig. 6b**), and the light current and dark current could be switched effectively, indicating a stable sequential optical response. In addition, the *I-V* curves of the flexible PDs arrays were determined under different bending cycles, as shown in **Fig. 6c** in logarithmic scale. After 10000 bending cycles, the photocurrent slightly decreased, probably due to an increase in electrode resistance, while the flexible PDs arrays continued to function normally. Long-period photoreaction measurements were also performed to analyze the stability of the device without encapsulation (room temperature, 30-45% relative humidity). The modified device could maintain almost the same magnitude of photocurrent and functioned normally after 100 days of storage under the same environmental conditions. The test conditions were consistent (excitation wavelength of 405 nm and power of 11.52 mW cm^{-2}), as shown in **Fig. 6d,** without any encapsulation and protection. The long-term stability of the photoresponse of the modified device is shown in **Fig. 6e**. The evolution of *R* shows that the modified device has significantly improved long-term stability and can retain more than 85% of its original value after 100 days of storage under ambient conditions. On the other hand, the *R* value of the original device (without PMMA) was only about 40% of its original value after 40 days. Therefore, the PMMA film on the top significantly improved the environmental stability of device, which was not the case for other devices with perovskite hybrid structure (**Fig. S15**). Remarkably, no significant photoelectric loss effect due to the PMMA film was observed in this work, as the untreated and PMMA-covered devices exhibited the same degree of photoresponsivity. The high photoelectric properties and better environmental stability have great potential advantages for a variety of applications, such as optical imaging and digital displays[2, 51].
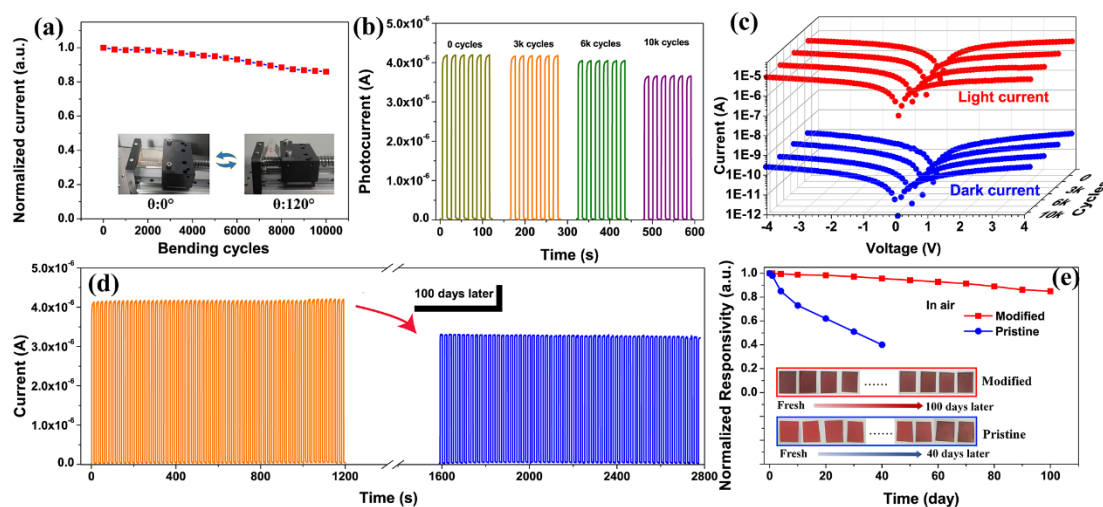
Fig. 6. Bending tolerance and air stability of flexible device. (a) Bending tolerance test for modified device. Inset are photographs of the device under different bending states. **(b)** and **(c)** *I-t* and *I-V* curves of the device after different bending cycles. **(d)** Photoresponse of the unencapsulated device in a test period of about 100 days (Bias voltage of 2 V and illumination power density of 11.52 mW/cm² at 405 nm). **(e)** Responsivity evolution of unencapsulated device over time under ambient air condition. The inset shows the optical images of the pristine and modified samples over time.

We have shown here that the flexible device has good mechanical robustness and extremely high photoelectric performance, which offers potential application in artificial vision sensing. The flexible PDs array for multi-point light distribution detection are schematically shown in **Fig. 7a**. Actually, it is very important to verify the uniformity of light response of all pixels under uniform illumination. To evaluate the feasibility of the integrated PDs arrays, the uniformity of the optical response of all 10×10 pixels was investigated. First, we checked the uniformity of all pixels by counting the output current. The PDs arrays were illuminated with homogenous white light (0.01 mW cm⁻²) and the dark current and photocurrent of each pixel were recorded separately. The photoresponse results are summarized in 2D comparison maps, with different colors representing different current levels in **Fig. 7b** and **7c**. The measurements confirmed that all detectors in the optical sensor were functional. In order to further confirm the reproducibility of the fabrication process, we prepared more than three 10×10 PDs arrays (**Fig. S16**). From the statistics of photocurrent and dark current of the three devices, we can see that the average values of photocurrent and dark current of each prepared device were almost the same, indicating that the device have high reproducibility. The dark current of most pixels was in the range of hundreds of picoamperes (pA) and the photocurrent was in the range of several tens of nanoamperes (nA) at a bias voltage of 2 V, indicating relatively satisfactory uniformity.
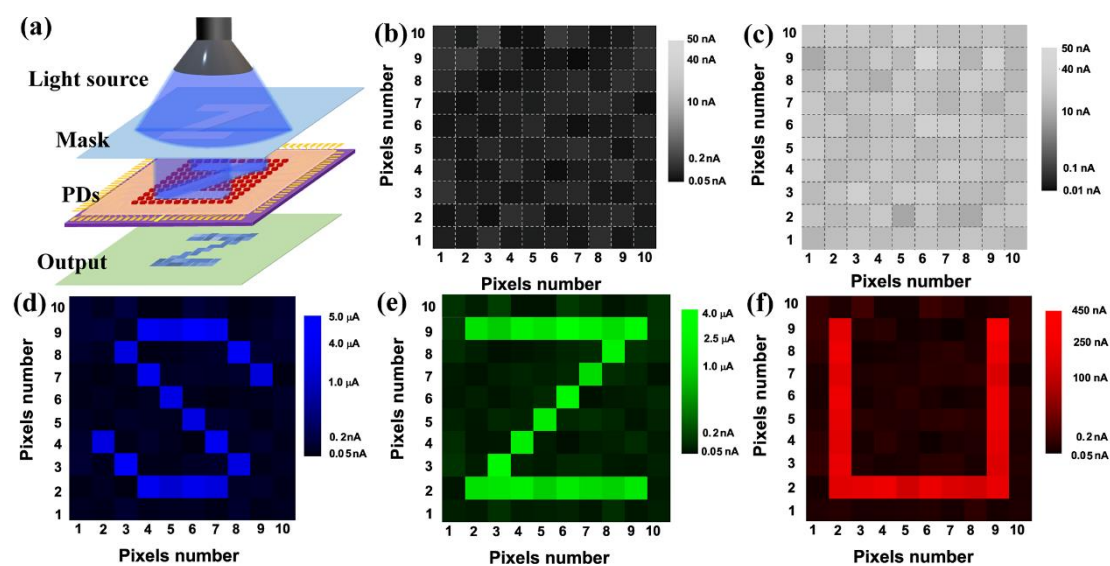
Fig. 7. Demonstration of the device for the light imaging capacity. (a) Schematic illustration of the flexible PDs arrays to detect multipoint light distribution. **(b)** and **(c)** 2D contrast maps showing the channel current of PDs arrays in the dark and under white light. **(d-f)** Photoelectric imaging results of "S", "Z", and "U" under blue (405 nm), green (532 nm), and red (808 nm) light, respectively.

The average dark current was ≈ 0.14 nA, and photocurrent was ≈ 38.6 nA, respectively (**Fig. S17b**). Although the device performance varies from pixel to pixel, the tendency of the dark and photocurrent to deviate from the mean was almost the same for each pixel device. The measured current variation for each pixel may be caused by fluctuation of the perovskite layer thickness in the PDs array.

In addition, the application of the device in light trajectory tracking and visible light imaging was studied. A prefabricated shadow mask was placed between the light source and the PDs array to form a small light point, as shown in **Fig. S17c**. The light point was moved from pixel to pixel by moving the mask, and the photoresponse of the illuminated PDs was immediately measured (**Fig. S17d**). It is noteworthy that each pixel operates independently without any electrical crosstalk between the pixels in the array. **Fig. S17e** shows that the current of the illuminated unit increased sharply while the other unit remained constant. The experimental results confirm that PDs arrays can accurately map the trajectory of light spots. In addition, the imaging capability of 10 × 10 addressable PDs arrays for a simple character was investigated. As shown in **Fig. 7d-f**, the pixel designing the hollow area of the letter had a large output photocurrent, while the other pixels blocked by the mask remained only at the dark current level. The channel current of each pixel was measured and then included in a 2D contrast current mapping. The letters "S", "Z", and "U", representing the logo of Shenzhen University, were clearly seen in the imaging results at 405 nm, 532 nm and 808 nm, respectively. This shows the great potential of the array as a broadband imager. However, it should be noted that the imaging performance in the NIR region is not as good as in the UV-visible region due to the

relatively weak quantum efficiency, which may be improved by using photonic engineering for instance. Thus, this means that the perovskite PDs arrays have preliminary imaging capability. The spatial resolution can be optimized by further reducing the size of the pixel device.

3. Discussion

In summary, we fabricated large-area flexible PDs arrays based on quasi-2D $(BA)_2FAPb_2I_7$ (n=2) perovskite by an improved bottom-up photolithography method. The introduction of Au_NPs and FACl recrystallization process reduced the defects and grain boundaries of the perovskite films, improved the crystallinity, and lowered the surface defects, enabling the device to achieve high-resolution imaging. The flexible PDs arrays exhibited excellent optoelectronic properties with a high responsivity of 5.48 A W^{-1}, a detectivity of 8.2×10^{12} Jones, an on/off current ratio of 3×10^4, and a broad spectral response. In addition, the device showed excellent electrical stability and folding strength under severe bending, as well as excellent operation stability with a slightly decreased photoresponse after 100 days of ambient storage (room temperature, 35-40% relative humidity). Moreover, the integrated 10×10 flexible PDs arrays were used as the sensor pixel of an imaging system to obtain high-resolution imaging patterns, demonstrating the imaging capability of the quasi-2D perovskite-based PDs arrays. Therefore, the fabricated devices have far-reaching potential for light sensing and imaging of artificial electronic skin and electronic eye, as well as for optical sensing of digital displays in the future.

4. Material and Methods

Materials

Lead iodide (PbI_2, 99.99%), butyliodide amine (butylammonium iodide, BAI, 99.5%), formamidinium iodide (FAI, 99.5%), FACl (99.5%) were purchased from Xi'an Polymer Light Technology Corp. N,N-dimethylformamide (DMF, anhydrous, 99.8%), dimethyl sulfoxide (DMSO, GC, 99.9%), isopropanol (C_3H_8O, AR, 99%), and chlorobenzene (C_6H_5Cl, AR, 99%) were purchased from Aladdin Chemical Reagent Co., Ltd. Hexane (C_6H_{14}, AR,97%, Macklin) and (octadecyl) trichlorosilane ($C_{18}H_{37}SiCl_3$, 95%,5-10% branched isomers, Macklin) were purchased from Baolet Technology Co., Ltd. Poly(methyl methacrylate) (PMMA, Macklin) were purchased from Guangtryan Reagent Technology Co., Ltd. All chemical compounds and reagents were used without any further purification.

Device Fabrication

First, the flexible PET substrates were ultrasonically cleaned with deionized water, ethanol, acetone, isopropanol, and ethanol for 20 min. They were then treated for 20 min by UV-ozone,

the electrodes were fabricated through UV lithography followed by a lift-off process. Cr/Au electrodes with the thicknesses of 10 nm/100 nm were prepared by radio frequency (RF) magnetron sputtering. Then, a layer of SiO_2 film (20 nm) was deposited by RF magnetron sputtering, which could be used as an assisted layer for surface hydrophobicity treatment. Third, the surface of SiO_2 film was treated with a 300:1 mixed solution of hexane and (octadecyl) trichlorosilane (OTS) for 20 min to render the whole surface hydrophobic [[1]], followed by washing with acetone to remove the photoresist, exposing the hydrophilic region of the array covered with the photoresist. After treatment, the substrate surface was hydrophilic in specific array regions and hydrophobic in other regions to facilitate the preparation of perovskite arrays. Subsequently, perovskite arrays were synthesized by solution spin coating. The precursor solution mixed 276.6 mg PbI_2, 120.6 mg BAI and 51.6 mg FAI in DMF and DMSO. It was spin-coated on the prepared substrate at 3000 rpm for 30 s and annealed at 100 °C for 15 s. After 15 s annealing, Au nanoparticles were sprayed for 15 s immediately (Au nanoparticles were sputtered on the surface of perovskite through an ion sputtering coater (ISC150, 10W)). The layer was then annealed for 20 min. After annealing, the samples were spin-coated with FACl solution (8 mg mL^{-1} in isopropanol) at 3000 rpm for 10 s and annealed at 100 °C for 10 min. Finally, the device was packaged by PMMA (20 mg mL^{-1} in chlorobenzene).

Characterizations and Measurements

The XRD data of samples were measured using high-resolution diffractometer (X'pertpro, 3 kW, 40 mA) with Cu Kα source radiation (λ = 0.154 nm). The UV–vis absorption spectra were acquired on a home-build optical setup (PerkinElmer LAMBDA spectrophotometer). The top of the PVK layer was excited by a 470 nm diode laser (Picoquant). The collected PL was filtered by a 488-nm long-pass filter, and analyzed for time-resolved photoluminescence decay on the glass substrate by a PerkinElmer SPCM avalanche photodiode combined with a Picoharp acquisition card (500 ps characteristic time of the total system response function) used with the laser in a pulsed mode at a 10 nW excitation power (pulse duration 70 ps). The morphology of perovskite films was obtained by SEM (GeminiSEM 560, 2 kV acceleration voltage). The UPS was measured by an ultraviolet photoelectron spectrometer (ThermoFisher Nexsa). GIWAXS measurements were performed with a microfocus X-ray source (IμS, Incoatec, Germany) generating Cu Kα radiation (λ=1.54 Å). GIWAXS patterns were acquired using a single photon counting 2D X-ray detector (Pilatus 100 K, Dectris, Switzerland) with an exposure time of 10 s. The angle of incidence was set to 2°, and the sample detector distance to 73 mm. GD-OES analysis was performed using a HORIBA Jobin Yvon GD Profiler 2 apparatus. The instrument was equipped with a RF-generator (13.56 MHz), a standard HORIBA Jobin Yvon glow discharge source, cylindrical anodes with an inner diameter of 4 mm, and two optical spectrometers (one polychromatic and one monochromator) for rapid optical detection. The argon plasma was generated at an argon pressure of 420 Pa and the applied power was 17 W.

The perovskite film was mounted on an O-ring on one side of the plasma chamber, which acts as a cathode. The analyzed perovskite film area was a disk 4 mm in diameter. The Au electrode was fabricated using UV lithography (MA605080104, Germany) and magnetron sputtering apparatus instrument (SP-LC6-A06, Acer Technology Co., Ltd). The *I-V* and *I-t* performance of the PDs were tested by Keithley 2614 B electrometer. The two probes were inserted into the interfinger electrodes on the device, and then irradiated by the laser diodes with wavelengths of 375, 405, 450, 532, 635, and 808 nm. The voltage ranged from -4 V to 4 V, and the interval was 0.1 V. A xenon lamp with a monochromator and laser diode was used as a light source for the PDs measurement. The irradiance power was adjusted from 0.27 μW cm^{-2} to 11.52 mW cm^{-2} using an optical attenuator and was measured by using a power meter.

Transfer-matrix simulation

The device was modeled optically by use of the transfer-matrix formalism. Introduction of AuNP within the PVK layer was treated within the effective-medium approximation, with an effective index of the PVK+Au_NPs medium given by the Maxwell-Garnett equation. The permittivity of the Au was obtained from Johnson and Christy, and the refractive index of perovskite was extracted from the literature[47].

Author contributions.

D.Z., L.C., T.P. and F.F. supervised the project. They conceived and designed the experiments. W.T. and D.Z. conducted most of the experiments. K.V., N.M. and P.S. helped to the analysis of the data and intervened in the manuscript writing and finalization. X.Y. and M.G.S. helped with data analysis. W.T. and D.Z. wrote the manuscript with input from all authors. All authors have given approval to the final version of the manuscript.

Competing interests.

The authors declare no competing interests.

References and Notes

[1] W. Wu, X. Wang, X. Han, Z. Yang, G. Gao, Y. Zhang, J. Hu, Y. Tan, A. Pan, C. Pan, Adv Mater, 31 (2019) e1805913.

[2] W. Wu, X. Han, J. Li, X. Wang, Y. Zhang, Z. Huo, Q. Chen, X. Sun, Z. Xu, Y. Tan, C. Pan, A. Pan, Adv Mater, 33 (2021) e2006006.

[3] W. Kong, F. Zeng, Z. Su, T. Wang, L. Qiao, T. Ye, L. Zhang, R. Sun, J. Barbaud, F. Li, X. Gao, R. Zheng, X. Yang, Advanced Energy Materials, 12 (2022) 2202704.

[4] H. Shao, X. Wu, D. Zhou, W. Chen, L. Li, W. Xu, L. Xu, B. Dong, X. Bai, H. Song, Small Methods, 6 (2022) e2200163.

[5] M. Piccardo, M. de Oliveira, A. Toma, V. Aglieri, A. Forbes, A. Ambrosio, Nature Photonics, 16 (2022) 359-365.

[6] D. Zheng, T. Zhu, Y. Yan, T. Pauporté, Advanced Energy Materials, 12 (2022) 2103618.

[7] D. Zheng, T. Zhu, T. Pauporté, Solar RRL, 5 (2021) 2100010.

[8] F.C. Daming Zheng, Marie-Noelle Rager, Liam Gollino, Boxue Zhang, Thierry Pauporté, Adv. Mater. Interfaces 9(2022) 2201436.

[9] J. Jang, Y.G. Park, E. Cha, S. Ji, H. Hwang, G.G. Kim, J. Jin, J.U. Park, Adv Mater, 33 (2021) e2101093.

[10] G. Cen, Y. Liu, C. Zhao, G. Wang, Y. Fu, G. Yan, Y. Yuan, C. Su, Z. Zhao, W. Mai, Small, 15 (2019) e1902135.

[11] M.-B. Lien, C.-H. Liu, I.Y. Chun, S. Ravishankar, H. Nien, M. Zhou, J.A. Fessler, Z. Zhong, T.B. Norris, Nature Photonics, 14 (2020) 143-148.

[12] J. Xue, Z. Zhu, X. Xu, Y. Gu, S. Wang, L. Xu, Y. Zou, J. Song, H. Zeng, Q. Chen, Nano Lett, 18 (2018) 7628-7634.

[13] L. Gu, S. Poddar, Y. Lin, Z. Long, D. Zhang, Q. Zhang, L. Shu, X. Qiu, M. Kam, A. Javey, Z. Fan, Nature, 581 (2020) 278-282.

[14] H.-J. Kim, H. Oh, T. Kim, D. Kim, M. Park, ACS Applied Nano Materials, 5 (2022) 1308-1316.

[15] K. Xia, W. Wu, M. Zhu, X. Shen, Z. Yin, H. Wang, S. Li, M. Zhang, H. Wang, H. Lu, A. Pan, C. Pan, Y. Zhang, Science Bulletin, 65 (2020) 343-349.

[16] G. Yang, K. Zhu, W. Guo, D. Wu, X. Quan, X. Huang, S. Liu, Y. Li, H. Fang, Y. Qiu, Q. Zheng, M. Zhu, J. Huang, Z. Zeng, Z. Yin, H. Wu, Advanced Functional Materials, 32 (2022) 2200457.

[17] X. Feng, Y. He, W. Qu, J. Song, W. Pan, M. Tan, B. Yang, H. Wei, Nat Commun, 13 (2022) 6106.

[18] L. Cheng, Z. Liu, S. Li, Y. Zhai, X. Wang, Z. Qiao, Q. Xu, K. Meng, Z. Zhu, G. Chen, Angew Chem Int Ed Engl, 60 (2021) 856-864.

[19] R. Dong, C. Lan, X. Xu, X. Liang, X. Hu, D. Li, Z. Zhou, L. Shu, S. Yip, C. Li, S.W. Tsang, J.C. Ho, ACS Appl Mater Interfaces, 10 (2018) 19019-19026.

[20] G.E. Eperon, S.D. Stranks, C. Menelaou, M.B. Johnston, L.M. Herz, H.J. Snaith, Energy & Environmental Science, 7 (2014) 982.

[21] C.M.M. Soe, C.C. Stoumpos, M. Kepenekian, B. Traore, H. Tsai, W. Nie, B. Wang, C. Katan, R. Seshadri, A.D. Mohite, J. Even, T.J. Marks, M.G. Kanatzidis, J Am Chem Soc, 139 (2017) 16297-16309.

[22] T. Leijtens, K.A. Bush, R. Prasanna, M.D. McGehee, Nature Energy, 3 (2018) 828-838.

[23] H. Wang, D.H. Kim, Chem Soc Rev, 46 (2017) 5204-5236.

[24] X. Huang, Q. Guo, D. Yang, X. Xiao, X. Liu, Z. Xia, F. Fan, J. Qiu, G. Dong, Nature Photonics, 14 (2019) 82-88.

[25] M.S. Alias, I. Dursun, D. Shi, M.I. Saidaminov, E.M. Diallo, D. Priante, T.K. Ng, O.M. Bakr, B.S. Ooi, Journal of Vacuum Science & Technology B, Nanotechnology and Microelectronics: Materials, Processing, Measurement, and Phenomena, 33 (2015) 051207.

[26] J. Liu, B. Shabbir, C. Wang, T. Wan, Q. Ou, P. Yu, A. Tadich, X. Jiao, D. Chu, D. Qi, D. Li, R. Kan, Y. Huang, Y. Dong, J. Jasieniak, Y. Zhang, Q. Bao, Adv Mater, 31 (2019) e1901644.

[27] C.Y. Wu, Z. Wang, L. Liang, T. Gui, W. Zhong, R.C. Du, C. Xie, L. Wang, L.B. Luo, Small, 15 (2019) e1900730.

[28] J. Wu, J. Chen, Y. Zhang, Z. Xu, L. Zhao, T. Liu, D. Luo, W. Yang, K. Chen, Q. Hu, F. Ye, P. Wu, R. Zhu, Q. Gong, Nano Lett, 17 (2017) 3563-3569.

[29] X. Geng, F. Wang, H. Tian, Q. Feng, H. Zhang, R. Liang, Y. Shen, Z. Ju, G.Y. Gou, N. Deng, Y.T. Li, J. Ren, D. Xie, Y. Yang, T.L. Ren, ACS Nano, 14 (2020) 2860-2868.

[30] B. Huang, J. Liu, Z. Han, Y. Gu, D. Yu, X. Xu, Y. Zou, ACS Appl Mater Interfaces, 12 (2020) 48765-48772.

[31] T. Wang, D. Zheng, J. Zhang, J. Qiao, C. Min, X. Yuan, M. Somekh, F. Feng, Advanced Functional Materials, 32 (2022) 2208694.

[32] N. Pellet, P. Gao, G. Gregori, T.Y. Yang, M.K. Nazeeruddin, J. Maier, M. Gratzel, Angew Chem Int Ed Engl, 53 (2014) 3151-3157.

[33] Y. Liu, S. Akin, A. Hinderhofer, F.T. Eickemeyer, H. Zhu, J.Y. Seo, J. Zhang, F. Schreiber, H. Zhang, S.M. Zakeeruddin, A. Hagfeldt, M.I. Dar, M. Gratzel, Angew Chem Int Ed Engl, 59 (2020) 15688-15694.

[34] J. Lu, T. Yang, T. Niu, N. Bu, Y. Zhang, S. Wang, J. Fang, X. Chang, T. Luo, J. Wen, Y. Yang, Z. Ding, K. Zhao, S. Liu, Energy & Environmental Science, 15 (2022) 1144-1155.

[35] H. Li, X. Shan, J.N. Neu, T. Geske, M. Davis, P. Mao, K. Xiao, T. Siegrist, Z. Yu, Journal of Materials Chemistry C, 6 (2018) 11961-11967.

[36] Y. Zhan, W. Chen, F. Yang, Y. Li, Chinese Physics B, 30 (2021) 088803.

[37] J. Wang, S. Luo, Y. Lin, Y. Chen, Y. Deng, Z. Li, K. Meng, G. Chen, T. Huang, S. Xiao, H. Huang, C. Zhou, L. Ding, J. He, J. Huang, Y. Yuan, Nat Commun, 11 (2020) 582.

[38] L. Lin, J.T.-W. Wang, T.W. Jones, M. Grigore, A. Cook, D.W. deQuilettes, R. Brenes, B.C. Duck, K.F. Anderson, N.W. Duffy, B. Wenger, V. Bulović, J. Pu, J. Li, B. Chi, H.J. Snaith, G.J. Wilson, Journal of Materials Chemistry A, 7 (2019) 25511-25520.

[39] T.H. Han, S. Tan, J. Xue, L. Meng, J.W. Lee, Y. Yang, Adv Mater, 31 (2019) e1803515.

[40] K. Wang, C. Wu, D. Yang, Y. Jiang, S. Priya, ACS Nano, 12 (2018) 4919-4929.

[41] Y. Chen, S. Tan, N. Zhou, N. Yang, W. Zhou, Y. Wu, K. Weber, Q. Chen, H. Zhou, Solar RRL, 3 (2019) 1900083.

[42] S. Chen, G. Shi, Adv Mater, 29 (2017) 1605448.

[43] M. Kim, G.-H. Kim, T.K. Lee, I.W. Choi, H.W. Choi, Y. Jo, Y.J. Yoon, J.W. Kim, J. Lee, D. Huh, H. Lee, S.K. Kwak, J.Y. Kim, D.S. Kim, Joule, 3 (2019) 2179-2192.

[44] Y.H. Lee, S. Park, Y. Won, J. Mun, J.H. Ha, J.H. Lee, S.H. Lee, J. Park, J. Yeom, J. Rho, H. Ko, J.H. Oh, NPG Asia Materials, 12 (2020) 79.

[45] D. Zheng, C. Schwob, Y. Prado, Z. Ouzit, L. Coolen, T. Pauporté, Nano Energy, 94 (2022) 106934.

[46] T. Wang, D. Zheng, K. Vegso, N. Mrkyvkova, P. Siffalovic, T. Pauporté, Advanced Functional Materials, (2023) 2304659.

[47] F. Feng, T. Wang, J. Qiao, C. Min, X. Yuan, M. Somekh, ACS Applied Materials & Interfaces, 13 (2021)61496-61505.

[48] S. Chen, C. Teng, M. Zhang, Y. Li, D. Xie, G. Shi, Adv Mater, 28 (2016) 5969-5974.

[49] Z. Ji, G. Cen, C. Su, Y. Liu, Z. Zhao, C. Zhao, W. Mai, Advanced Optical Materials, 8 (2020) 2001436.

[50] Z. Liu, X. Liu, B. Sun, X. Tan, H. Ye, J. Zhou, Z. Tang, T. Shi, G. Liao, Advanced Materials Technologies, 5 (2020) 2000260.

[51] B. Xia, M. Tu, B. Pradhan, F. Ceyssens, M.L. Tietze, V. Rubio-Giménez, N. Wauteraerts, Y. Gao, M. Kraft, J.A. Steele, E. Debroye, J. Hofkens, R. Ameloot, Advanced Engineering Materials, 24 (2021) 2100930.

[52] Y. Li, Z. Shi, L. Lei, S. Li, D. Yang, D. Wu, T. Xu, Y. Tian, Y. Lu, Y. Wang, L. Zhang, X. Li, Y. Zhang, G. Du, C. Shan, Advanced Materials Interfaces, 6 (2019) 1900188.

[53] W. Deng, X. Zhang, L. Huang, X. Xu, L. Wang, J. Wang, Q. Shang, S.T. Lee, J. Jie, Adv Mater, 28 (2016) 2201-2208.

[54] J. Qiao, F. Feng, S. Song, T. Wang, M. Shen, G. Zhang, X. Yuan, M.G. Somekh, Advanced Functional Materials, 32 (2021) 2110706.

[55] R. Pan, H. Li, J. Wang, X. Jin, Q. Li, Z. Wu, J. Gou, Y. Jiang, Y. Song, Particle & Particle Systems Characterization, 35 (2018) 1700304.

[56] S. Tong, J. Sun, C. Wang, Y. Huang, C. Zhang, J. Shen, H. Xie, D. Niu, S. Xiao, Y. Yuan, J. He, J. Yang, Y. Gao, Advanced Electronic Materials, 3 (2017) 1700058.

[57] R. Nasanen, H. Ojanpaa, T. Tanskanen, J. Paallysaho, Exp Brain Res, 172 (2006) 464-471.

[58] K. Rayner, T.J. Smith, G.L. Malcolm, J.M. Henderson, Psychological science, 20 (2009) 6-10.

[59] J. Ghosh, G. Natu, P.K. Giri, Organic Electronics, 71 (2019) 175-184.

[60] Q. Gu, C. Hu, J. Yang, J. Lv, Y. Ying, X. Jiang, G. Si, Materials & Design, 198 (2021) 109374.

[61] C. Li, Z. Liu, Q. Shang, Q. Zhang, Advanced Optical Materials, 7 (2019) 1900279.

[62] C. Ma, D. Zheng, D. Demaille, B. Gallas, C. Schwob, T. Pauporté, L. Coolen, Solar Energy Materials and Solar Cells, 230 (2021) 111144.

[63] M.A. Haque, S. Kee, D.R. Villalva, W.L. Ong, D. Baran, Adv Sci (Weinh), 7 (2020) 1903389.

[64] Y. Wang, R. Lin, P. Zhu, Q. Zheng, Q. Wang, D. Li, J. Zhu, Nano Lett, 18 (2018) 2772-2779.

[65] A. Pisoni, J. Jacimovic, O.S. Barisic, M. Spina, R. Gaal, L. Forro, E. Horvath, J Phys Chem Lett, 5 (2014) 2488-2492.

[66] Q. Li, S. Wang, M. Zhang, L. Feng, X. Su, W. Ding, Y. Li, F. Yun, Solar Energy, 173 (2018) 590-596.

[67] K. Dong, H. Zhou, M. Xiao, P. Gui, Z. Gao, F. Yao, W. Shao, C. Liu, C. Tao, W. Ke, Applied Physics Letters, 120 (2022) 191102.

[68] J.C. Fan, F.J. Bachner, G.H. Foley, P.M. Zavracky, Applied Physics Letters, 25 (1974) 693-695.

[69] D. Zheng, F. Raffin, P. Volovitch, T. Pauporte, Nat Commun, 13 (2022) 6655.

[70] G. Murugadoss, R. Thangamuthu, M.R. Kumar, Materials Letters, 230 (2018) 270-274.

[71] Y. Wang, X. Liu, L. Li, C. Ji, Z. Sun, S. Han, K. Tao, J. Luo, Chem Asian J, 14 (2019) 1530-1534.

[72] B. Hwang, J.S. Lee, Advanced Optical Materials, 7 (2018) 1801356.

[73] R. Dong, C. Lan, F. Li, S. Yip, J.C. Ho, Nanoscale Horizons, 4 (2019) 1342-1352.

[74] D. Yu, F. Cao, Y. Gu, Z. Han, J. Liu, B. Huang, X. Xu, H. Zeng, Nano Research, 14 (2020) 1210-1217.

[75] Y. Zhao, C. Li, J. Jiang, B. Wang, L. Shen, Small, 16 (2020) e2001534.

[76] C. Fang, H. Wang, Z. Shen, H. Shen, S. Wang, J. Ma, J. Wang, H. Luo, D. Li, ACS Appl Mater Interfaces, 11 (2019) 8419-8427.

[77] R.K. Ulaganathan, R.C. Murugesan, C.Y. Lin, A. Subramanian, W.L. Chen, Y.M. Chang, A. Rozhin, R. Sankar, Advanced Functional Materials, (2021) 2112277.

[78] T. Ji, H. Zhang, N. Han, W. Wang, B. Wu, G. Li, M. Fan, Z. Li, Y. Hao, F. Zhu, Y. Wu, Y. Cui, Journal of Materials Chemistry C, 8 (2020) 1110-1117.

ToC

The authors present a method to prepare quasi-2D Ruddlesden-Popper halide perovskite layers (n = 2) of high structural quality, pixelized on a polyethylene terephthalate (PET) flexible substrate. The process enables a deposition on a large scale, in a controllable manner. They prepare flexible PDs arrays with good spatial resolution, excellent optoelectronic properties, high responsivity, and high stability.